This is the accepted version of the following article

Mohd Zahid Ansari, Petr Janicek, Dip K. Nandi, Karel Palka, Stanislav Slang, Deok Hyun Kim, Taehoon Cheon, Soo-Hyun Kim (2021). Influence of post-annealing on structural, optical and electrical properties of tin nitride thin films prepared by atomic layer deposition. *Applied Surface Science.* Volume 538. DOI: 10.1016/j.apsusc.2020.147920

Publisher's version is available from:
https://www.sciencedirect.com/science/article/pii/S0169433220326775

This version is licenced under a Creative Commons Attribution-NonCommercial-NoDerivatives 4.0.International.

Influence of post-annealing on structural, optical and electrical properties of tin nitride thin films prepared by atomic layer deposition

Mohd Zahid Ansari[a], Petr Janicek[b,c,*], Dip K. Nandi[a], Karel Palka[c,d], Stanislav Slang[c], Deok Hyun Kim[a,e], Taehoon Cheon[e], Soo-Hyun Kim[a,f,*]

[a] School of Materials Science and Engineering, Yeungnam University, 280 Daehak-Ro, Gyeongsan, Gyeongbuk 38541, Republic of Korea
[b] Institute of Applied Physics and Mathematics, Faculty of Chemical Technology, University of Pardubice, Studentska 95, Pardubice 532 10, Czech Republic
[c] Center of Materials and Nanotechnologies, Faculty of Chemical Technology, University of Pardubice, Studentska 95, Pardubice 532 10, Czech Republic
[d] Department of General and Inorganic Chemistry, Faculty of Chemical Technology, University of Pardubice, Studentska 95, Pardubice 532 10, Czech Republic
[e] Center for Core Research Facilities, Daegu Gyeongbuk Institute of Science & Technology, Sang-ri, Hyeonpung-myeon, Dalseong-gun, Daegu 711-873, Republic of Korea
[f] Institute of Materials Technology, Yeungnam University, Yeungnam University, 280 Daehak-Ro, Gyeongsan, Gyeongbuk 38541, Republic of Korea

A R T I C L E I N F O

Keywords:
Atomic layer deposition
Tin nitride
Post annealing
Optical properties
Ellipsometry analysis

A B S T R A C T

Post-thermal annealing treatment is an effective process employing the thin film structure modifications and compositional properties. In this article, we present a detailed investigation and understanding of the changes in the phase, crystal structure, microstructure, and optoelectrical properties of tin nitride (SnN_x) thin films. These were deposited by atomic layer deposition (ALD) followed by annealing at temperatures ranging from 300 to 550 °C. The results suggest that post-annealing significantly influences the properties of as-deposited ALD SnN_x thin films at 150 °C. For instance, X-ray diffractometry (XRD) and transmission electron microscopy (TEM) results demonstrate that the as-deposited film predominantly forms an amorphous structure. After annealing up to 350 °C, the film retains its amorphous structure with a minor enhancement in crystallinity. The bonding state to reveal its phase was confirmed by X-ray photoelectron spectroscopy (XPS). The as-deposited film predominantly forms SnN bonding from Sn^{2+} states, and it is changed after annealing at 350 °C, where the fraction of Sn^{4+} from the Sn_3N_4 phase considerably increases. However, the XRD and TEM results do not distinguish the differences between as-deposited or 300 °C -annealed and 350 °C-annealed samples. After the annealing temperature is increased to 400 and 450 °C, both processes of crystallization into the mixed phase of hexagonal SnN and cubic Sn_3N_4, and their decomposition into metal Sn with simultaneous nitrogen release occur. At a further elevation of the annealing temperature (500 °C and beyond), a considerably distorted morphology and agglomeration of the as-deposited film structure was observed. This was due to the formation of island-like structures or droplets of metallic Sn by significantly releasing (or almost all) the nitrogen within the films. As the film properties vary upon annealing, spectroscopic ellipsometry (SE) was used to investigate the optical and electrical parameters of the as-deposited and annealed films. The optical band gap of the as-deposited film is 1.5 eV and remains unchanged up to 400 °C; it then increases to 1.9 eV at higher annealing temperatures. The electrical resistivity of the films decreases monotonically as the annealing temperature increases, which is attributed to the change in carrier concentration. The change in the optoelectronic properties can be associated with the change in crystallinity and escape of the nitrogen content connected with the change in stoichiometry.

1. Introduction

Metal nitride (MN_x) thin films are drawing considerable attention in many research fields due to their versatile physical and chemical properties [1]. Transition metal nitrides (TMNs) are a vital part of this family due to their thermal and chemical stabilities and suitable electrical properties, especially for integrated circuit (IC) fabrication. Several other MN_x [such as Si_3N_4, AlN, GaN, Zn_3N_2, and SnN_x, most of which are also known as post-transition metal nitrides (post-TMNs)] are also of immense importance [2–4]. MN_x possess a wide range of

bandgaps, leading to the formation of metallic nitrides as well as semiconductors and even insulators, with important applications in optoelectronic devices [3–6]. Moreover, several MNs such as SnN_x, TiN_x, VN_x, and MoN_x have been successfully investigated as heterogeneous catalysts and electrodes for rechargeable energy storage devices [7–13]. Tin nitride (SnN_x) is considered an emerging earth-abundant post-transition metal nitride for several applications such as vapor ethanol sensing, energy storage, microelectronics, and recording media devices due to its attractive electronic and electrochromic properties [12–20].

Many methods have been pursued to prepare tin nitride thin films, including chemical vapor deposition (CVD), plasma-enhanced CVD, magnetron, or radio-frequency (RF) sputtering [15–28]. Among these, RF sputtering is the most frequently used technique to grow tin nitride thin films from tin in a nitrogen-containing atmosphere. Investigation of the prepared thin films was mainly focused on crystallographic features, chemical bonding nature, and surface structure considering the different processing conditions. For example, Inoue *et al.* reported on SnN_x films fabricated by reactive sputtering, which showed an n-type semiconductor with mobilities of ~3 cm^2/Vs and carrier densities of approximately 10^{20} cm^{-3} [17]. The sputtered SnN_x film prepared from a Sn target with an Ar and N_2 plasma mixture forms tin nitride films and changes in crystallinity with partial metal Sn as a function of the flow rate of N_2 gas in the gas mixture [5]. However, these fabrication methods are line-of-sight deposition and do not guarantee excellent uniformity and conformance of the deposit on very complex nano- or 3D-structures with high aspect ratios. Recently, we reported a new preparation method for SnN_x thin films by atomic layer deposition (ALD) at low temperatures (70–200 °C) where the precursor and reactant are alternately pulsed into the reaction chamber one at a time, separated by purging with inert gases. The film is formed by the self-limited surface reaction between them [7]. Due to their ideal ALD characteristics, ALD-SnN_x films grew uniformly on very narrow sized 3-dimensional features with ~100% step coverage, and they were successfully utilized as free-standing electrodes in electrochemical supercapacitors and Li-ion batteries.

Furthermore, several TMNs and post-TMNs undergo considerable physical changes (such as phase change, including amorphous to crystalline conversion) during post-deposition heat treatment (annealing) [29–33]. Numerous studies have been performed on ALD grown nitrides (such as MoN_x, WN_x, TaN_x, HfN_x, *etc.*), where the phase change (from amorphous to crystalline) and the decomposition of the nitride film to metal were observed after annealing [36–41]. For example, the amorphous δ-MoN films deposited by sputtering at room temperature, crystallized after annealing in vacuum at temperatures above 600 °C [36]. In another study, the sample annealed at a temperature lower than 650 °C exhibited a *y*-Mo_2N phase with a face-centered-cubic (FCC) structure having smaller grains, and a tetragonal structure Mo_2N phase with larger grain sizes was obtained at higher post-annealing temperatures of 700 and 900 °C [37]. Similarly, a cubic W_2N film deposited by reactive sputtering was stable up to 700 °C and at 800 °C, a mixture phase of W and W_2N was formed, which was further converted to pure W [38]. The sputter-deposited TaN_x thin film underwent a remarkable phase transformation from Ta_4N to Ta_2N, and its surface morphology buckled and agglomerated as the annealing temperature increased from 350 to 500 °C [39]. The post-annealing of these films also leads to decomposition of the respective nitride materials (generally at a high temperature) by releasing N [40]. Therefore, while post-annealing is necessary for enhancing the properties of most metal nitride thin films, a detailed study of these annealed films is also essential. In this context, it is important to investigate the thermal stability of the ALD SnN_x thin films by annealing the samples at different temperatures.

Here, we investigate the physical and optoelectronic properties of the as-deposited and annealed ALD-SnN_x films at different temperatures. While annealing enhances the crystallinity and other properties of the as-deposited SnN_x films, its potential decomposition at higher temperatures was studied in detail. Since there are no studies on the optoelectronic behavior of ALD-SnN_x films, a significant portion of this study is dedicated to probing these properties with the help of spectroscopic ellipsometry (SE). SE provides information on several optical parameters, such as the refractive index (*n*), extinction coefficient (*k*), and bandgap (E_g), and electronic characteristics (carrier density, mobility, etc.) of as-deposited and annealed SnN_x films.

2. Materials and methods

2.1. Materials preparations

SnN_x thin films were fabricated in a travelling-wave type ALD reactor (Lucida-D100, NCD technology), using tetrakis (dimethylamino) tin {TDMASn, $[(CH_3)_2N]_4Sn$}, and ammonia (NH_3) at a deposition temperature of 150 °C. The temperature of TDMASn was maintained at 40 °C to provide sufficient vapor pressure (~0.3 Torr) for the deposition. In addition, highly purified Ar gas was used as a carrier gas at a controlled flow rate (100 sccm) for enabling the smooth delivery of the TDMASn precursor into the reaction chamber. Si wafers covered with thermally grown SiO_2 (~100 nm) were used as substrates to grow the SnN_x films. High-purity Ar gas was used to purge the excess chemicals and reaction byproducts from the reactor between each sequential precursor pulse. The basic pulsing recipe that ensures the self-limiting growth of the SnN_x films was set as follows: 5 s pulsing of TDMASn precursor, 10 s purging with Ar gas, 5 s pulsing of NH_3, and 10 s purging with Ar. Further details of the growth kinetics can be found in our previous report [7]. After successfully fabricating the SnN_x thin films using ALD, they were annealed in vacuum for 30 min using rapid thermal annealing (RTA) at a working pressure of ~0.006 Torr. The annealing process was carried out at six different temperatures ranging from 300 to 550 °C, with 50 °C steps. The temperatures at which these films were annealed define the nomenclature used throughout the study as SnN-300, SnN-350, SnN-400, SnN-450, SnN-500, and SnN-550, respectively.

2.2. Material characterization

A variety of characterization techniques were used to analyze the SnN_x films before and after annealing. Changes to the crystal structure and phase were analyzed using grazing incident angle (incident angle: 3°) X-ray diffraction (GIAXRD, PANalytical X'-pert PRO MRD with Cu Kα source at 1.5 kW) within 2θ of 10–90°. Since SnN_x thin films were deposited using a metal-organic precursor (TDMASn) and ammonia (NH_3), the as-grown film is expected to contain a considerable amount of hydrogen (H) due to its presence in the precursor. Therefore, the amount of hydrogen in the as-deposited film and post-annealed sample at 400 °C was measured by elastic recoil detection analysis (ERDA). ERDA was accomplished using Cl ions at a 6 MeV acceleration energy equipped with an ion accelerator (National Electrostatic Corp., NEC-6SBH). The presence of constituent elements and their respective oxidation states in the as-grown and annealed SnN_x films were studied by X-ray photoelectron spectroscopy (XPS, ESCALAB 250 spectrometer at the Korea Basic Science Institute Busan, Korea) using an Al K_α source. The morphology and thickness of each film were observed by plane view or top view and cross-sectional-view field-emission scanning electron microscopy (SEM, Tescan LYRA 3) at an acceleration voltage of 10 kV. Atomic force microscopy (AFM, Solver NEXT, NT-MDT, in a semi-contact mode) was used to examine the surface topography and roughness of all the films being studied. Plan-view and cross-sectional-view transmission electron microscopy (TEM, Tecnai F20 equipped with a 200-kV accelerating voltage and field emission gun) was used to capture bright-field or high-resolution images to elucidate the microstructure and crystal lattice of the as-grown and annealed SnN_x films in detail.

2.3. Ellipsometry analysis

Optical characterizations of the as-grown and annealed ALD-SnN_x films were carried out using two variable-angle spectroscopic ellipsometers (VASE and IR-VASE, J. A. Woollam Co.). The first, a rotating analyzer ellipsometer, operates in the spectral range of 190–1700 nm [ultraviolet–visible-near-infrared (UV–Vis-NIR)]. Measurements of each sample were performed during 25 analyzer revolutions with photon energy steps of 0.05 eV at four selected angles of incidence (AOI) at 50°, 55°, 60°, and 65°. Second, a rotating compensator ellipsometer, covers a 1.7–12 μm spectral range [NIR-MIR (mid-infrared)] for the same angle of incidence were recorded (measuring 25 scans, 15 spectra per revolution, with wavenumber steps of 8 cm^{-1}). Near-normal incident optical reflectance was measured using the same instruments. The WVASE32 software was used to model the measured data. The five-layer model consisted of Si, SiO_2, ALD-SnN_x layer, surface roughness, and air as ambient. The optical constants for Si and SiO_2 were acquired from the literature [50]. The Bruggeman effective medium approximation with 50% ALD-SnN_x and 50% air was utilized for surface roughness modeling [45,51]. A homogenous layer was used for the representation of the ALD SnN_x layer, as the atomic layer deposition is known to produce uniform layers [34,35].

3. Results and discussion

3.1. Phases and microstructures of as-grown and annealed ALD-SnN_x films

SnN_x thin films were prepared by ALD using the optimized dosing conditions (5 s-10 s-5 s-10 s) at a substrate temperature of 150 °C, which assured the self-limited growth behavior of the films. Fig. 1 shows the GIXRD patterns of the as-deposited SnN_x and SnN_x thin films after post-annealing at different temperatures. As shown in Fig. 1, all the XRD patterns can be indexed either to a mixed-phase or an individual phase of cubic tin nitride (Sn_3N_4) (space group: Fd$\overline{3}$m), hexagonal tin nitride (SnN) (space group: P$\overline{3}$m1), and metallic beta-tin (Sn) (space group: $I4_1$/amd). The reference JCPDS data of their respective phases are also included at the bottom of Fig. 1. It is worth mentioning that only two SnN_x crystal structures of SnN/SnN_x (hexagonal) and Sn_3N_4 (cubic) were prepared and reported in the literature [43]. A broad hump at approximately ~32.2° in the XRD results from analyzing the as-deposited SnN_x film indicates that a nanocrystalline structure formed close to the predominantly amorphous one, and the center of the hump could be ascribed to the (1 0 1) plane of hexagonal SnN or the (3 1 1) plane of cubic Sn_3N_4. The predominant amorphous phase of the as-deposited film was further confirmed by TEM analysis, as described later. However, a highly polycrystalline film was successfully formed after annealing. However, slight improvements in crystallinity were observed up to 350 °C; beyond this, distinct and sharp XRD peaks with high intensity could be ascribed to mixed-phase tin nitride. In addition, the increasing presence of the Sn metal phase at higher annealing temperatures could be identified along with the tin nitride mixed-phase. At a post-annealing temperature of 450 °C, the diffraction peaks from both tin nitrides were observed more clearly than at any other annealing temperature. Owing to the complex peak characteristics and similar interplanar spacing (or 2θ values) of cubic tin nitride (Sn_3N_4) and hexagonal tin nitride (SnN), clear indexing is, however, not straightforward. In addition, some nominal peak shifts may have appeared because of the concurrence of different phases (influence in lattice parameters for Sn by SnN_x and vice versa, for example, note the peak related to Sn at ca. 63°). This further complicates the XRD data. Interestingly, at the highest temperature (500–550 °C) under consideration, the as-deposited tin nitride films were completely transformed into metallic tin islands and no continuous film remained, suggesting that all N was released from the films.

To obtain further detailed information on the microstructure, crystal structure, and morphology, we performed cross-sectional view TEM (XTEM) analysis of the as-deposited and annealed SnN_x films. The low-magnification bright-field (BF) XTEM images shown in Fig. S1 [Fig. S1 (a) and (c)] for the as-deposited and SnN-350 samples clearly show the formation of a continuous, smooth, uniform film over a large area of interest by ALD. Only a slight change was observed in the microstructure by annealing at relatively low-temperature. The high-magnification XTEM images [Fig. S1 (b) and (d)] further show that the contrast of the image does not seem to be uniform, indicating the spatial formation of tin nitrides with different Sn/N ratios. The predominant amorphous nature of the as-deposited film and SnN-350 sample is shown in the high-resolution (HR) TEM images [Fig. 2(a, b) and Fig. 2(c, d)] and complemented with the diffuse ring patterns of the

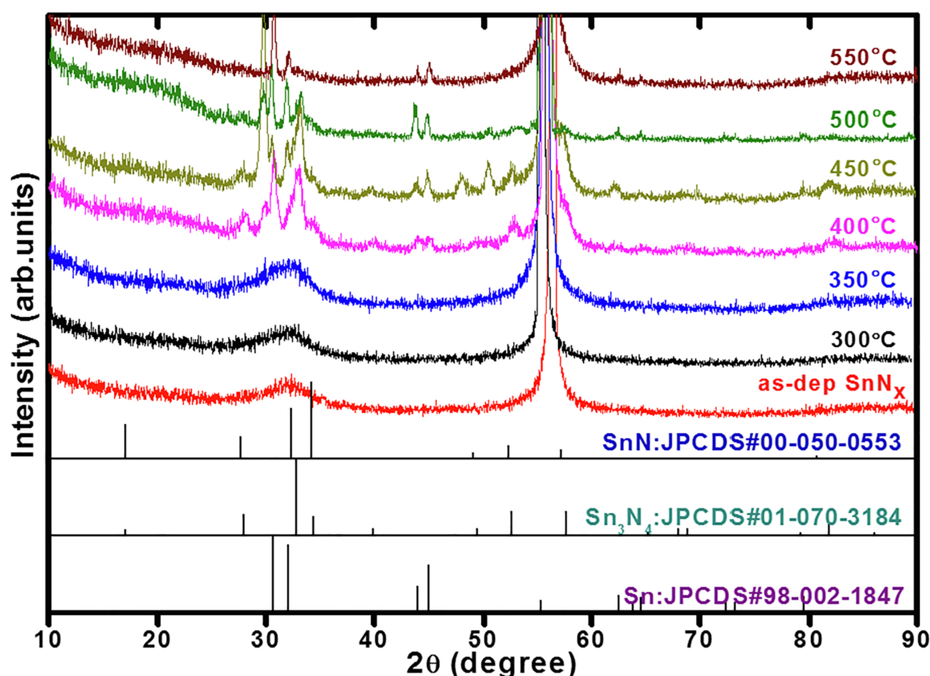

Fig. 1. XRD spectra of ALD-SnN_x films as-deposited temperature at 150 °C and as a function of the annealed at 300, 350, 400, 450, 500 and 550 °C.

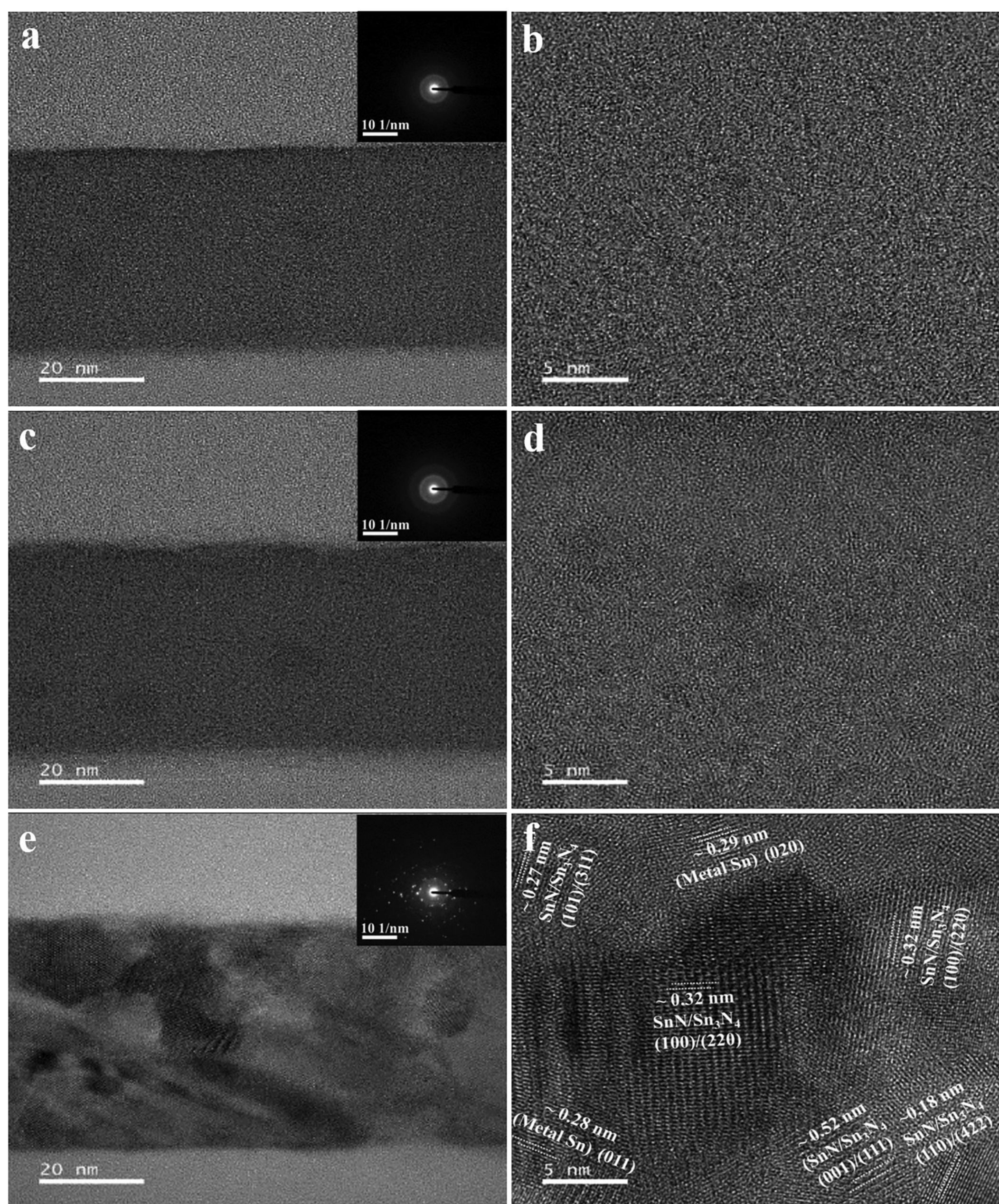

Fig. 2. Cross-sectional view TEM micrographs and their corresponding HRTEM images with SAED patterns of the (a, b) as-deposited SnN_x at 150 °C, post-annealing at (c, d) 350 °C, and (e, f) 450 °C.

same by selected area electron diffraction (SAED) analysis [the insets of Fig. 2(a) and (c)]. However, the SnN-450 sample clearly shows well-defined crystalline features in the HR-TEM images, as shown in Fig. 2(e, f), while its surface is still smooth. The lattice fringe spacing observed at several different positions was measured, and the estimated d-spacing could be designated as the corresponding planes of different phases. The observed lattice spacing belongs to the different crystalline planes of both hexagonal SnN and cubic Sn_3N_4 as well as the structure of the metal Sn. These lattice spacing measurements are well matched to the values of the JCPDS references of hexagonal SnN or cubic Sn_3N_4 (JCPDS# 50-0553, & 70-3184) and even metallic tin (JCPDS# 02-1847). Moreover, the highly polycrystalline films could also be investigated from the SAED pattern with bright diffraction spots [inset of Fig. 2(e)] of the SnN-450 sample. Thus, the TEM results are in good agreement with the XRD results showing the stability of the amorphous dominant as-deposited film. Complete crystallization into the mixed phase of hexagonal SnN and cubic Sn_3N_4 occurs upon annealing above 400 °C. The dominant Sn metal droplet formation above 500 °C, and TEM provides the microstructural change of ALD- SnN_x by annealing. However, it is still difficult to determine which phases are dominant depending on the annealing temperature due to the overlapping of the diffraction peaks from both phases.

XPS analysis was performed to confirm the constituent elements, composition, and oxidation states of the Sn and N species, revealing the phase formation before and after annealing the SnN_x films. The complete XPS surveys (0–1000 eV) obtained with and without Ar+ sputtering of the as-deposited SnN_x films and the films annealed at different temperatures are presented in Figure S2. Several peaks corresponding to different orbital electrons of Sn (Sn 3s, 3p, 3d, and 4d) could be easily identified in the full XPS survey spectra of the samples. In addition, peaks corresponding to N 1s, O 1s, C 1s, and Si 2p were also observed with different intensities in different samples, before and after sputtering. While O and C appeared as surface contamination, Si and O were detected from the substrate for the films annealed at high temperature.

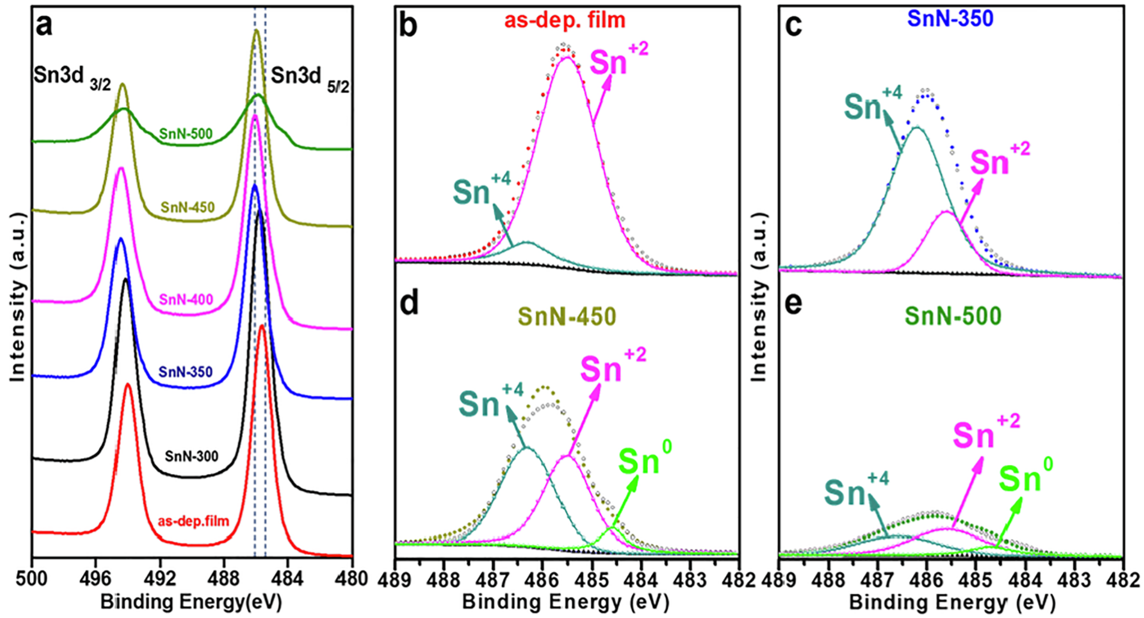

Fig. 3. (a) High-resolution XPS spectra of the Sn 3d electronic states in the SnN_x films, and corresponding deconvolution of the Sn $3d_{5/2}$ peaks of (b) SnN-150, (c) SnN-350, (d) SnN-450, and (e) SnN-500.

There is a higher atomic percentage of C and O on the surface of the film for both as-deposited and annealed films before Ar-sputtering, which significantly reduced after sputtering, confirming these elements as surface contamination. Furthermore, the atomic percentage of N was significantly higher after Ar sputtering. Therefore, the further high-resolution spectra of Sn 3d and N 1s were investigated in detail for the XPS that was recorded after Ar sputtering to eliminate the unwanted O and C impurities from the surface of the samples. The high-resolution XPS core level spectra of the Sn 3d region of the SnN_x films grown at 150 °C, annealed at 300–500 °C [Fig. 3(a)], and the illustrative deconvolution of the individual Sn $3d_{5/2}$ electronic states of as-deposited SnN_x annealed at 350, 450, and 500 °C are displayed in Fig. 3(b)–(e). Based on XPS measurements of the Sn 3d spectra of the Sn-based nitrides, the principal oxidation states of SnN and Sn_3N_4 surfaces are stated to be +2 and +4, respectively. The peak intensities of the Sn 3d spectra of the SnN_x films were almost identical to the as-deposited film after they were annealed at temperatures up to 450 °C and significantly decreased after annealing at 500 °C as shown in Fig. 3(a). Interestingly, the shift in the peak maxima shown by the dotted line in the Sn $3d_{5/2}$ XPS peak in Fig. 3(a) as we compared the peak shift those of the as-deposited SnN_x to those of films annealed at different temperatures. The peak is gradually shifted to a higher binding energy (BE), possibly due to the increased formation of the Sn_3N_4 phase upon annealing. The dominant form of Sn metal droplets due to nitrogen release once again shifts the peak maxima slightly towards the lower BE value after annealing at 500 °C. To obtain more evidence of the valence state of Sn, the Sn $3d_{5/2}$ spectra were de-convoluted by Gaussian fitting, and a similar outcome was expected for Sn $3d_{3/2}$.

The results show that the as-deposited SnN_x film at 150 °C (SnN-150) and post-annealed at 350 °C [Fig. 3(b) and (c)] exhibited two different components and are fitted by their respective sub-peaks that correspond to Sn^{+2} and Sn^{+4} positions at corresponding Sn $3d_{5/2}$ binding energies of approximately ~485.5 eV and ~486.3 eV, respectively [5,12,19,46,47]. From these observations, we notice a major and strong peak for the Sn^{+2} state in the SnN-150 sample and the Sn^{+4} state present in the SnN-350 sample. Thus, the increase in the Sn_3N_4 bonding in the SnN_x film upon annealing at 350 °C is evident from this XPS analysis, although both XRD and TEM analyses do not show any significant differences between the two samples. When the annealing temperature increased to 450 °C, the peak intensity from Sn^{+4} decreased while the additional bonding status from Sn (0) was newly detected at ~484.6 eV, which corresponds to Sn–Sn metal bonding in the SnN_x film [Fig. 3(d) and (e)]. For the SnN-500 sample, the overall intensity was significantly decreased and the de-convoluted results indicated that the decrease of the Sn^{+4} peak was more prominent compared to that of the Sn^{+2} peak. The peak intensity from Sn (0) increased with increase in annealing temperature to 500 °C.

Further, the high-resolution XPS spectra of N 1s are shown in Fig. 4(a), and the corresponding de-convoluted N 1s region of SnN-150 (as-deposited), SnN-350, SnN-450, and SnN-500 samples (annealed) are presented in Fig. 4(b–e). Similar to the Sn3d spectra, the peak intensities were almost constant for the as-grown and annealed films up to 450 °C and then decreased at elevated temperatures due to the N release from the samples. However, the peak signals shifted marginally towards higher BE first and then again shifted towards lower BE because of the change in the Sn-N bonding status. The de-convoluted N 1s spectra clearly shows two sub-peaks, the first part is located at higher BE of ~397.3 eV and can be ascribed to a SnN_x phase with Sn^{+2} valence, while the second constituent at lower BE of ~396.6 eV is indexed to the Sn^{+4} states from Sn_3N_4 [19,42–44]. In the SnN-500 sample, one additional peak located at a higher binding energy of ~400 eV assigned to N 1s in NO_2 might come from molecularly chemisorbed N_2 with leftover oxygen during post-annealing or upon exposure of the samples to ambient conditions. Similar observations were also made earlier, where it was reported that the oxygen in the sputtering chamber might also cause the formation of NO_2^- [5,49]. The de-convoluted N 1s spectra supports the Sn 3d XPS results. In the case of the SnN-150 sample, two N components from the bonding to form SnN and Sn_3N_4 are obvious, while the intensity from the former is higher. When the annealing was performed at 350 °C, the peak from Sn_3N_4 became much stronger, indicating the increase in Sn_3N_4 bond formation in the film. It is also interesting to note that in the SnN-450 and SnN-500 samples, the intensity of the N 1s peak was substantially reduced. This might be due to thermal decomposition when N atoms combine to form N_2 molecules and are released from the samples at higher annealing temperatures. The XPS result for the SnN-450 sample shows a significant decrease in the peak intensity from the Sn_3N_4 bonding, indicating that the decomposition of the SnN_x film mainly started from the cubic Sn_3N_4 phase. These observations suggest that the phase change in the SnN_x films upon annealing is obvious, leading to the formation of island-like

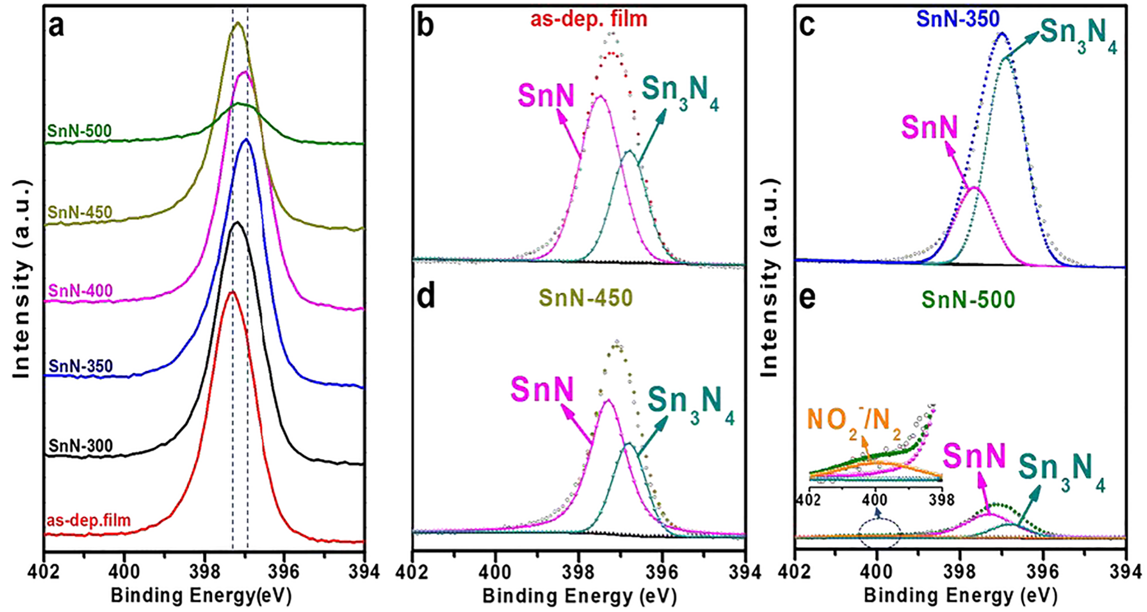

Fig. 4. (a) High-resolution N 1s XPS spectra of the as-grown SnN_x films as a function of vacuum annealing temperatures, and resultant peaks of deconvoluted N 1s (b) SnN-150, (c) SnN-350, (d) SnN-450, and (e) SnN-500.

metal Sn at high temperatures. This agrees with observations on SnN and other metal nitride reported in earlier studies [37–39,43,46–48].

The XPS results in this study are particularly interesting to elucidate the phase change of SnN_x with the increasing annealing temperature because the XRD and TEM do not show any clear differences between the phase changes owing to the complex peak appearances and very close interplanar spacing (or 2θ values) of Sn_3N_4 and SnN. Similar results have been reported by Caskey *et al.*, in their study, sputtered Sn nitride thin films showed a pair of distinct Sn 3d spectra corresponding to Sn^{+2} and Sn^{+4} oxidation states due to the mixed phase present in the film [19]. There are studies in the literature that report that the metastability was proven by Auger electron spectroscopy or XPS analysis, and that it disassociates into the metal element upon annealing under specific treatment conditions, and that decomposition starts between 420 °C and 615 °C (γ-Sn_3N_4 shows stability in a vacuum up to 300 °C) [15,17,18,23,24,43,47]. Due to its poor stability, it is rather difficult to define the exact stoichiometry of tin nitride films, because of the spontaneous oxidation, decomposition, and sputter damage when sputter-cleaned prior to XPS. Therefore, it is difficult to determine the exact physical characteristics of SnN_x from a research study [43]. Finally, the estimated atomic percentages of different states of tin nitride reveal that Sn^{+2} is predominantly present in the SnN-150 and SnN-350 samples compared to Sn^{+4}, whereas the SnN-450 and SnN-500 samples have Sn^{+4} species with an equivalent amount of Sn^{+2} and a considerable amount of metallic Sn. The atomic percentages of these different Sn oxidation states in the as-grown film and after annealing at different temperatures are presented in Table S1. Hydrogen, which may also exist in the films due to the use of H-containing metalloganic Sn precursor in this study, cannot be detected by XPS analysis due to no core electrons in H. Therefore, we further measured hydrogen content in the as-deposited film and after post-annealing at 400 °C using elastic recoil detection analysis (ERDA) (Fig. 5). ERDA results clearly detected the incorporation of hydrogen in the as-deposited film and the hydrogen content was significantly reduced after annealing. From the simulation of ERDA signal, a high concentration of ~11 at. % H was confirmed in the as-deposited SnN_x film. However, the hydrogen content significantly decreased to ~4 at. % when annealed at 400 °C.

The surface morphology of the tin nitride films of both as-deposited and annealed samples that were vacuum-annealed at various temperatures were studied via plane view and cross-sectional view SEM, as shown in Fig. 6 & S3 and S4. The first observation, arising from the cross-sectional and plane view SEM (Fig. S3 and S4) images, is that surfaces of the as-deposited and SnN_x films annealed up to 350 °C are continuous, smooth, extremely uniform, and compact (pin-hole free). Comparatively, the surface annealed above 350 °C gradually becomes rougher and discontinuous. Therefore, an annealing temperature of 400 °C and above degrades the structure of the film because of the metal Sn droplets formation by the decomposition of the Sn_3N_4 phase. Furthermore, the samples annealed at 500 and 550 °C revealed a significantly distorted morphology and agglomeration of the film's substance, leading to large islands of the metal Sn rather than forming a continuous film. Such drastic changes are caused by the decomposition to metal Sn droplets (releasing N_2). Eventually, a considerable amount of the substrate is exposed in the post-annealed films in Fig. 6 (d, e, and f), which may limit their use depending on the voids/holes that can be tolerated. The Si 2p XPS peak assigned to SiO_2, the substrate, is observed in the films annealed only above 400 °C, confirming the partial exposure of the substrate (Figure S5). No peak corresponding to Si could be detected for the as-grown film or in the films that were annealed up to 400 °C. However, the Si 2p signal drastically increased when the film was annealed at 500 °C, suggesting a significant portion of the exposed SiO_2 wafer.

To obtain further insights, we examined the surface topography of the as-deposited films and the films annealed at various temperatures using AFM. The scans presented in Figs. [S6 (a-f)] show that the films annealed up to 400 °C have a dense and homogenous grain size distribution covering the complete surface of the substrate. The root mean square (RMS) surface roughness of all these SnN_x samples was estimated over a different area of interest (0.5 μm × 0.5 μm) on each sample, and the obtained values were plotted and are shown in Fig. S7. The average RMS roughness values of ~0.4 ± 0.09, 0.9 ± 0.16, 0.6 ± 0.03, 0.8 ± 0.12, and 2.9 ± 0.07 nm were obtained for SnN-150, SnN-300, SnN-350, SnN-400, and SnN-450, respectively. These values drastically increased at a relatively high annealing temperature

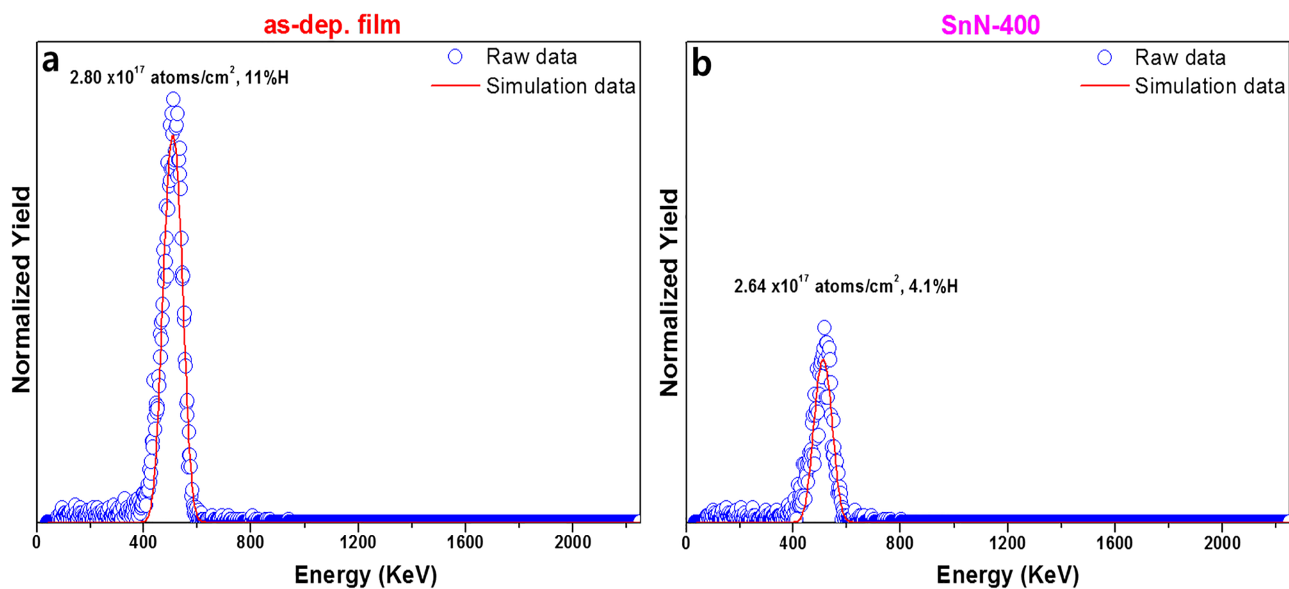

Fig. 5. Experimental and simulated ERDA spectra of ALD-SnN_x thin films; (a) as-deposited film at 150 °C and (b) post-annealed one at 400 °C.

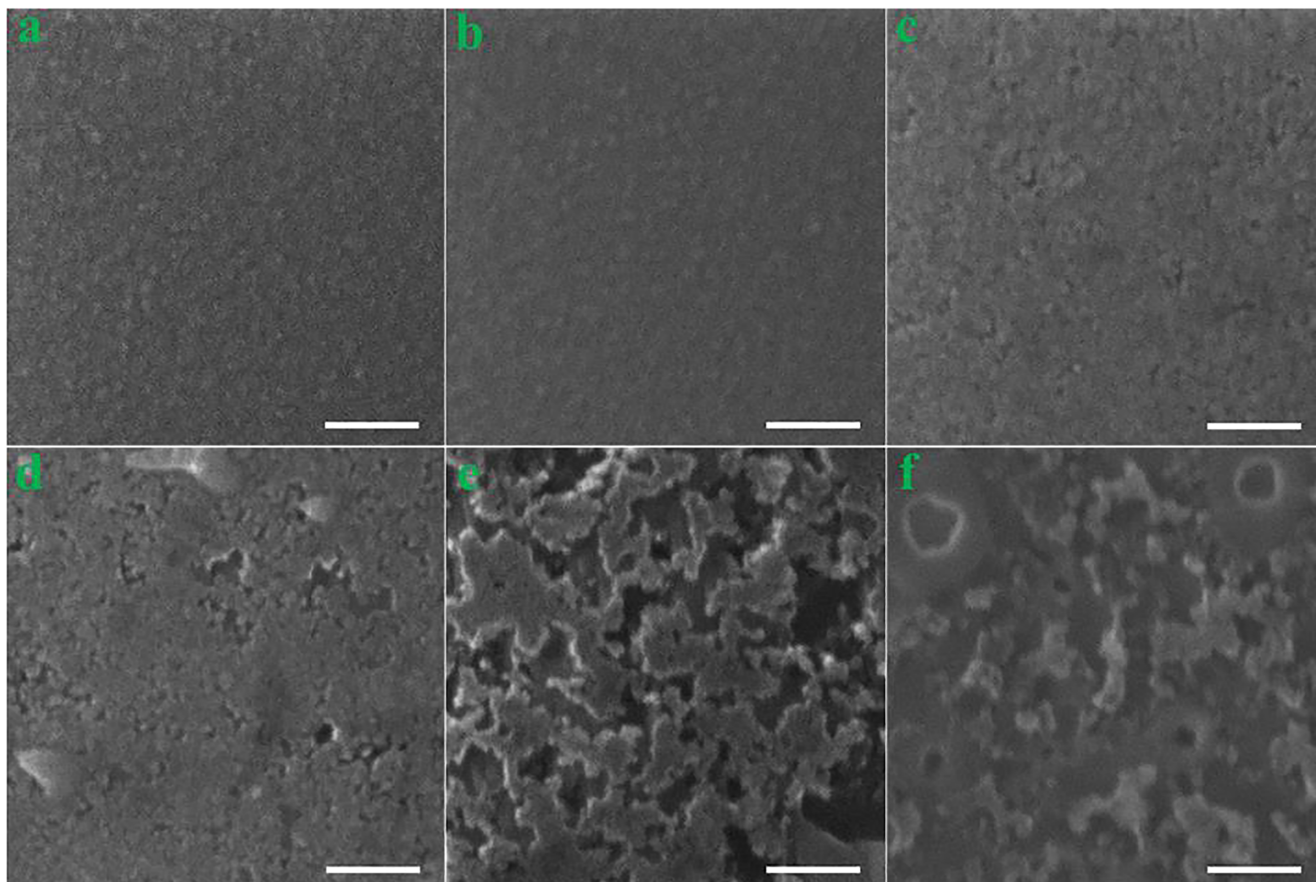

Fig. 6. Plane view SEM images of ALD-SnN_x films on thermally grown SiO_2 on Si wafer (a) as-deposited film at 150 °C and followed by different annealing temperature at (b) 350 °C, (c) 400 °C, (d) 450 °C, (e) 500 °C, and (f) 550 °C (All the scale bars are equivalent to 100 nm).

(data not shown) due to significant agglomeration of the film into island-like metal Sn. Therefore, these observations are similar to the changes in microstructure observed by XRD and TEM, where the as-grown and annealed samples up to 350 °C are amorphous or amorphous-like in nature. When the annealing temperature was increased to 400 and 450 °C, the simultaneous occurrence of both the crystallization of hexagonal SnN and cubic Sn_3N_4 mixed phase was observed. The initiation of their decomposition, lead to nitrogen

Table 1
Thickness of SnN_x layer as-grown and post-annealed at 300, 350, 400, 450, 500 and 550 °C in a vacuum, surface roughness and mean square error (MSE) obtained from the best fit of the ellipsometry data.

Sample	As-dep.	SnN-300	SnN-350	SnN-400	SnN-450	SnN-500	SnN-550
Layer thickness (nm)	44.1 ± 0.2	48.6 ± 0.1	45.8 ± 0.1	40.2 ± 0.3	36 ± 0.3	34.1 ± 0.5	6 ± 4
Surface roughness (nm)	2.9 ± 0.1	3.3 ± 0.1	4.0 ± 0.1	10.7 ± 0.3	8.9 ± 0.3	0.9 ± 0.5	15 ± 4
MSE	4.5	4.0	3.7	2.3	2.5	5.1	3.2

dissipation from the film. As the annealing temperature increases to 500 and 550 °C, nitrogen dissipation becomes more severe, resulting in the predominant formation of Sn droplets and morphology degradation. Thus, the alteration in microstructural parameters and surface morphology of the post-annealed films has been demonstrated, with the analysis of their post-annealed optoelectrical properties described in the following section.

3.2. Optical and electrical properties of as-deposited and annealed ALD-SnN_x films based on SE analysis

If we consider the similarities in their results from the previous section, the spectral dependence of the ellipsometry parameters ψ and Δ can be divided into three groups. Group (A) is first formed by the as-deposited sample and samples annealed at 300 °C and 350 °C. For these three samples, a Tauc-Lorentz oscillator [52] described the short-wavelength absorption edge, and a Drude oscillator [53] described the absorption of free electrons. In the second group (B), samples were annealed at 400 and 450 °C, and in the third group (C), samples were annealed at 500 and 550 °C with the sum of the Lorentz oscillators to model the dielectric functions of both (B + C). Examples of the measured ellipsometry parameters ψ and Δ and the parameters obtained by the best fit for the SnN-300, SnN-450, and SnN-500 samples are shown in Fig. S8 of the supplementary materials. The mean square error (MSE) between the measured and modeled ellipsometry data, which shows the quality of the fit, is summarized in Table 1. The obtained optical constants will be discussed in the subsequent section. The thickness of the SnN_x layer together with the surface roughness obtained from the best fit of the ellipsometry data is also presented in Table 1. There is a clear trend showing a decrease in layer thickness with increasing annealing temperature to temperatures higher than 350 °C. The increased surface roughness for the SnN-400, SnN-450, and SnN-550 (data not shown) samples is consistent with the AFM results. For samples annealed at temperatures higher than 400 °C, non-uniformity higher than 5% is revealed. The highest thickness non-uniformity (15%) was found in the SnN-400 sample.

The similarity of the ellipsometry parameters suggests a similarity of optical constants for the samples in each group. The differences in the ellipsometry parameters among these groups suggests differences in the optical constants among these groups. Therefore, the optical constants are presented in the same groups. The dependence of the refractive index and extinction coefficient on wavelength is presented in Fig. 7 for the samples in group A – the first line (as-deposited, SnN-300, and SnN-350), group B – second line (SnN-400 and SnN-450), and group C – third line (SnN-500 and SnN-550), respectively. The results obtained for group A (Fig. 7 first line) are close to the results previously published for the same material using 300 ALD cycles [7]. This suggests that the optical constants are nearly independent of the layer thickness. The extinction coefficient increases together with the refractive index increase for longer wavelengths [Fig. 7(B)], suggesting that the layer conductivity increase is probably due to nitrogen being released from the layer, as discussed in the previous section. The SEM analysis displays clear morphology degradation for the SnN-500 and SnN-550 samples into Sn droplets [see Fig. 6(e-f)], and therefore it is questionable if the homogenous layer model gives realistic results for these samples [Fig. 7(C)]. Another proof of the low reliability of the optical constants determined for the samples in group C (SnN-500 and SnN-550) is that the refractive index for 632 nm is significantly lower than the value (~2.7) obtained for the other samples in our previous study [7]. Conversely, the decrease in the value of the refractive index for the samples in group C could be explained by the degradation of the layer morphology, as mentioned earlier.

To determine the indirect optical bandgap, the Tauc plot presented in Fig. 8 in the form of the dependence of $(\alpha E)^{1/2}$ on photon energy is usually used where $\alpha = \frac{4\pi k}{\lambda}$. The energy bandgap can be estimated as the intersection of the linear extension of this dependence and the energy axis (see dashed lines in Fig. 8). For samples annealed at temperatures higher than 400 °C [Fig. 8(B) and (C)] there is absorption across the entire measured spectral range (see also the right column for [Fig. 7(B) and (C)]. The values of the energy bandgap determined by considering intervals of increase in the absorption coefficient are summarized in Table 2. Please note that samples annealed at temperatures of 400 °C and higher are absorbing across the entire measured spectral range. Considering that the error in determining the energy bandgap (E_g) by the described methodology is approximately 0.1 eV, the energy bandgap ~of 1.5 eV does not significantly change with annealing temperatures up to 400 °C (see Table 2). It is also approximately the same as that reported in our previous study [7], and it is also similar to the energy bandgap values of SnN_x prepared by different deposition methods, as reported earlier [17,24,54]. Theoretical calculations predict a direct bandgap of 1.40 eV for spinel γ-Sn_3N_4 [54]. Further increases in the annealing temperature cause increases in the energy bandgap (samples Sn-450 and Sn-500). Although the value of the energy bandgap of nanocrystals can be influenced by the degree of crystallinity [56], in this case, we ascribe changes in the energy bandgap to a decrease in the nitrogen content connected with the change in stoichiometry. The energy bandgap and the refractive index values for the SnN-550 sample are probably unrealistic as the layer morphology is destroyed (see Fig. 6f).

If all thicknesses are fixed to the values summarized in Table 2, the refractive index and extinction coefficient for each wavelength can be fitted (using a point-by-point fit). A comparison of the optical constants near the short-wavelength edge obtained by the Tauc–Lorentz oscillator and by point-by-point fit can be found in Fig. S9 in the supplementary materials. Generally, these results are extremely similar, confirming the appropriateness of the Tauc-Lorentz oscillator for describing the short-wavelength absorption edge for the as-deposited sample and the SnN-300 and SnN-350 samples. As previously mentioned, the sum of the Lorentz oscillators was used for samples annealed at temperatures of 400 °C and higher.

When determining the free carrier concentration and mobility or the specific electrical resistivity and mean free time, a simple Drude oscillator [53] can be used. The results obtained using a single Drude oscillator for longer wavelengths ($>$ 1500 nm) with an effective mass

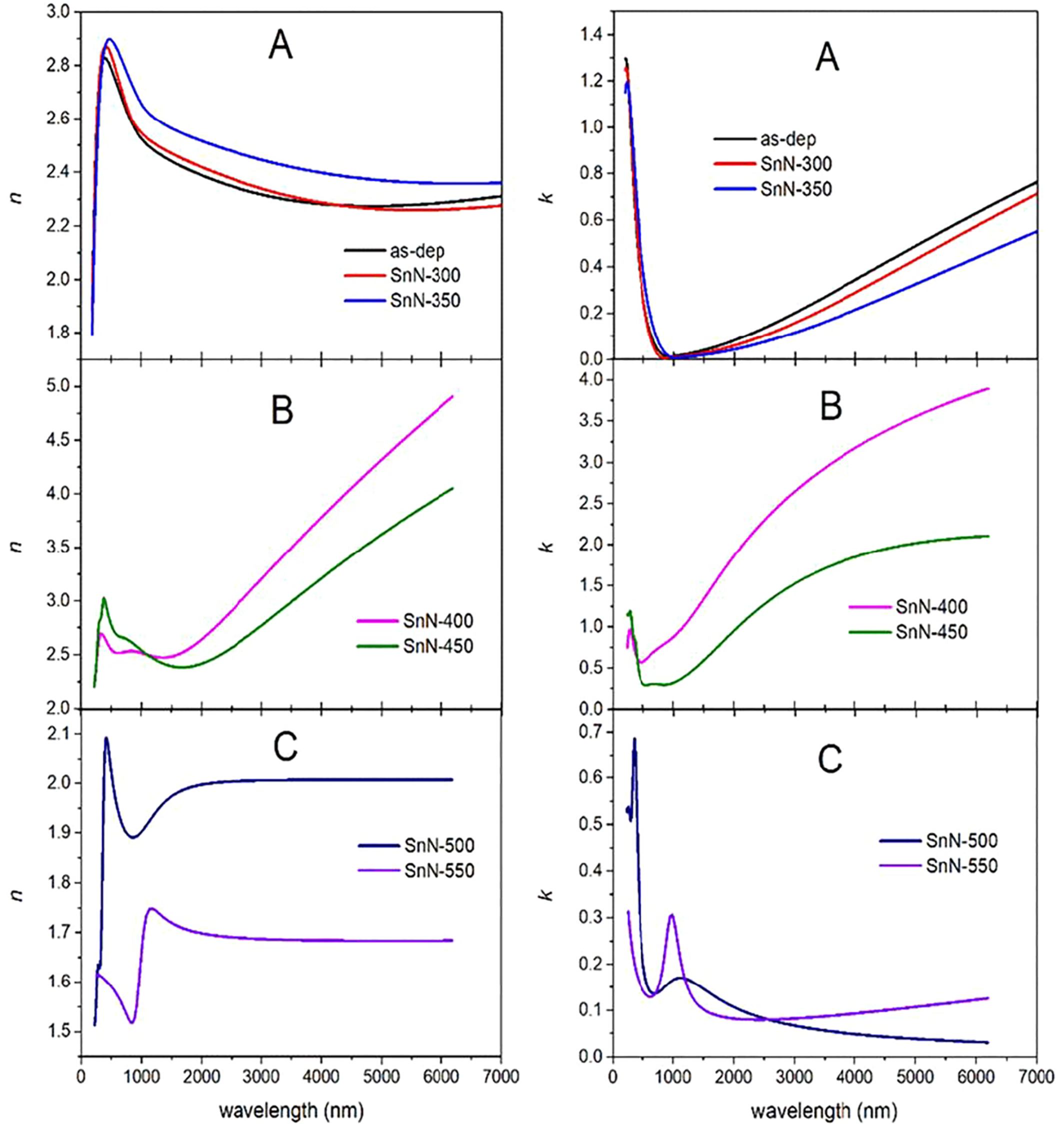

Fig. 7. Determined refractive index n (left column) and extinction coefficient k (right column) of SnN_x as-deposited (black) and post annealed for different temperatures (300 °C – red, 350 °C – blue, 400 °C – magenta, 450 °C – green, 500 °C – dark blue, and 550 °C – violet) as a function of wavelength. (For interpretation of the references to colour in this figure legend, the reader is referred to the web version of this article.)

equal to $0.17 \cdot m_{electron}$ [54] are summarized in Table 2. Free carrier concentrations of the order of 10^{19} cm^{-3}, mobility of the order 10^2 cm^2 V^{-1} s^{-1}, and resistivity of the order ~of 10^{-2} Ω·cm obtained for samples in group A are close to those reported in our previous work [7]. There is a visible decrease (both the decreases mentioned are by one order) in the specific electrical resistivity of group A (~10^{-2} Ω·cm for as-deposited and samples annealed at 300 and 350 °C) and group B (~10^{-3} Ω·cm for samples annealed at 400 and 450 °C) followed by a subsequent decrease in specific electrical resistivity for group C(~10^{-4} Ω·cm for samples annealed at 500 and 550 °C). The decrease in free carrier mobility between samples in group A (~10^2 cm^2 V^{-1} s^{-1}) and samples in group B (~10^1 cm^2 V^{-1} s^{-1}) together with the decrease in mean free time by one order is, can be attributed to the more frequent scattering of free carriers on grain boundaries induced by the higher degree of crystallinity confirmed by XRD. As previously mentioned, the model of the homogenous layers for the samples annealed at 500 and 550 °C is probably invalid. In this regard, one still notices high values for free carrier mobility and mean free time, suggesting conductive behavior for these samples. The comparison of optical constants determined in this range by using a simple Drude oscillator, a Lorentz oscillator, and point-by-point fit can be found in the supplementary materials' Fig. S10. From this comparison, it is clear that the Lorentz oscillator describes absorption for longer wavelengths better than the Drude oscillator does, we still view the trends in Table 2 considering the results from other methods.

All the results obtained from the spectroscopic ellipsometry support the results obtained by other methods shown in the previous section. This demonstrates that the crystallinity of the as-deposited amorphous or nanocrystalline (close to amorphous) ALD-SnN_x film was initially enhanced by annealing, and the resulting films were stable up to 350 °C. However, the films started to decompose into metal Sn and fully crystallized into hexagonal SnN and cubic Sn_3N_4, from approximately 400 °C. At further elevated temperatures (500 °C and beyond), the as-deposited film converts predominantly into island-like metal Sn

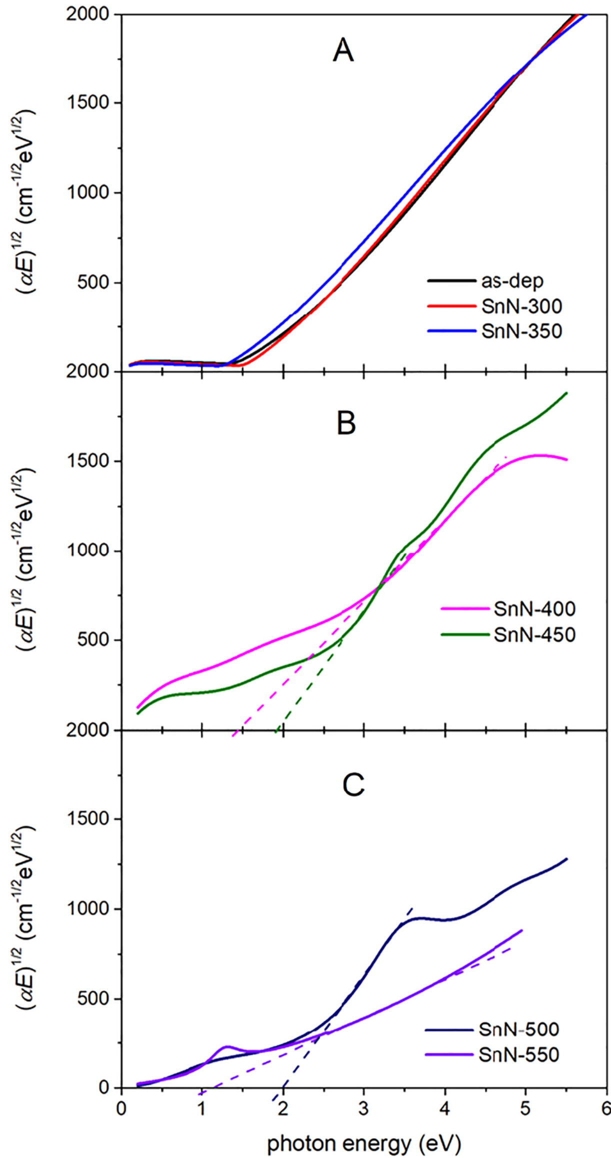

Fig. 8. $(\alpha E)^{1/2}$ as a function of photon energy (Tauc plot) for SnN_x as-deposited (black) and post annealed layers for different temperatures (300 °C – red, 350 °C – blue, 400 °C – magenta, 450 °C – green, 500 °C – dark blue, and 550 °C – violet). Dashed lines are used to determine the energy bandgap. (For interpretation of the references to colour in this figure legend, the reader is referred to the web version of this article.)

droplets by releasing N from the layer. It is necessary to note that considering the results of the previous section, an alternative model can be used for SnN_x post-annealed at 500 and 550 °C. In this model, the effective medium approximation [51,55] of Sn and voids are used. Using only two free parameters (the percentage of voids ineffective media approximation (EMA) and thickness of the layer), one can obtain a 54-nm thick layer that is 80% void for the SnN-500 sample and more realistically a 21-nm thick layer with 86% void for the SnN-550 sample. Although MSE is relatively high (41 for SnN-500 and 21 for SnN-550), this approach offers reasonable results, at least for samples post-annealed at 550 °C.

4. Conclusions

In this study, we investigated the effects of post-annealing on the thermal stability and optoelectronic properties of ALD-SnN_x thin films deposited at 150 °C using TDMASn and NH_3. Based o a complementary analysis using XRD, TEM, XPS, and SEM, the changes in crystallinity, microstructure, bonding states, and phases of the ALD-SnN_x film after post-annealing could be surmised at annealing temperatures ranging from 300 to 550 °C. First, the as-deposited SnN_x film forms a dominantly amorphous structure, where two Sn–N bonds (or two Sn oxidation states) are mixed, while it mainly consists of SnN (Sn^{2+}) bonding. The amorphous or amorphous-like structure was maintained without noticeable crystallization up to 350 °C annealing temperature. However, a slight improvement in the crystallinity by this low-temperature annealing significantly changes the Sn-N bonding status in the film, and the proportion of the Sn_3N_4 bonding is drastically increased. After annealing at 400 °C and 450 °C, the XRD and TEM results show the full crystallization of the SnN_x film into a mixture phase of hexagonal SnN and cubic Sn_3N_4 crystal structure. At these annealing temperatures, the decomposition of SnN_x also starts, and Sn metal forms mainly from the decomposition of the Sn_3N_4 phase. When the samples were annealed at temperatures above 500 °C, most of SnN and Sn_3N_4 decomposed, and nitrogen dissipation became more severe. This resulted in the predominant formation of the metal Sn islands and morphology degradation. The spectral dependence of the refractive index and the extinction coefficient resulting from the SE measurements further qualitatively supports the observations and conclusions explained above. The optical band gap of the as-deposited film is 1.5 eV and remains unchanged up to an annealing temperature of 400 °C and increases to 1.9 eV at higher temperatures. In addition, SE measurement was found to be successful in precisely assessing the thickness of a semiconducting ALD-SnN_x film and its surface roughness. All these outcomes suggest that alteration in crystallinity and composition upon post-annealing will have a great impact on the fundamental semiconductor and optoelectronic properties of ALD-SnN_x thin films. These will offer additional insight into the materials chemistry of tin nitride and other MN_x groups.

Table 2
Determined energy bandgap (E_g), free carrier concentration (n), free carrier mobility (μ), specific electrical resistivity (ρ) and mean free time (τ) for as-deposited and post annealed SnN_x samples. Please note that samples annealed with temperatures of 400 °C and above absorb across the whole measured spectral range and a simple Drude oscillator was used to determine n, μ, ρ, and τ (*the homogenous layer model is probably invalid).

Sample	E_g (eV)	n (10^{19} cm^{-3})	μ (cm^2/(Vs))	ρ (mΩ·cm)	τ (fs)
As-dep.	1.5 ± 0.1	3.3 ± 0.3	13 ± 2	15 ± 2	1.5 ± 0.2
SnN-300	1.5 ± 0.1	2.3 ± 0.3	17 ± 2	15 ± 2	1.9 ± 0.2
SnN-350	1.4 ± 0.1	1.4 ± 0.3	22 ± 2	20 ± 2	2.5 ± 0.2
SnN-400	1.4 ± 0.1	170 ± 20	4 ± 1	1.0 ± 0.2	0.4 ± 0.2
SnN-450	1.9 ± 0.1	170 ± 20	2 ± 1	2.1 ± 0.2	0.2 ± 0.2
SnN-500*	1.9 ± 0.1	1.9 ± 0.1	2000 ± 1000	0.12 ± 0.05	300 ± 100
SnN-550*	1.1 ± 0.1	0.8 ± 0.1	5000 ± 3000	0.10 ± 0.05	1000 ± 500

CRediT authorship contribution statement

Mohd Zahid Ansari and Soo-Hyun Kim purposed the research ideas, designed the experiments, and original draft preparation. Petr Janicek conducted the ellipsometry analysis and contributed to the writing and editing the manuscript. Karel Palka, and Stanislav Slang conducted the SEM and AFM analysis. Deok Hyun Kim, and Taehoon Cheona, conducted TEM analysis. Dip K Nandi reviewed and edited the manuscript. Soo-Hyun Kim supervised the research, reviewed, and modified the article. All authors contributed critically to the manuscript and gave final approval for publication.

Declaration of Competing Interest

The authors declare that they have no known competing financial interests or personal relationships that could have appeared to influence the work reported in this paper.

Acknowledgement

This work was financially supported by a grant from the Advanced Technology Center (ATC) Program (#10077265) funded by the Ministry of Trade, Industry & Energy (MOTIE) of the Republic of Korea. The authors appreciate the financial support from grant LM2018103 by the Ministry of Education, Youth, and Sports of the Czech Republic.

Appendix A. Supplementary data

Supplementary data to this article can be found online at https://doi.org/10.1016/j.apsusc.2020.147920.

References

[1] Y.u. Zhong, X. Xia, F. Shi, J. Zhan, J. Tu, H.J. Fan, Transition metal carbides and nitrides in energy storage and conversion, Adv. Sci. 3 (5) (2016) 1500286, https://doi.org/10.1002/advs.201500286.

[2] M.-S. Balogun, W. Qiu, W. Wang, P. Fang, X. Lu, Y. Tong, Recent advances in metal nitrides as high-performance electrode materials for energy storage devices, J. Mater. Chem. A 3 (4) (2015) 1364–1387.

[3] H. Kim, Atomic layer deposition of metal and nitride thin films: current research efforts and applications for semiconductor device processing, J. Vac. Sci. Technol. B 21 (6) (2003) 2231, https://doi.org/10.1116/1.1622676.

[4] T.D. Boyko, A. Hunt, A. Zerr, A. Moewes, Electronic structure of spinel-type nitride compounds Si_3N_4, Ge_3N_4, and Sn_3N_4 with tunable band gaps: application to light emitting diodes, Phys. Rev. Lett. 111 (2013) 097402, https://doi.org/10.1103/PhysRevLett.111.097402.

[5] S. Choi, J. Kang, J. Park, Y.-C. Kang, Tin nitride thin films fabricated by reactive radio frequency magnetron sputtering at various nitrogen gas ratios, Thin Solid Films 571 (2014) 84–89.

[6] J. Sato, N. Saito, Y. Yamada, K. Maeda, T. Takata, J.N. Kondo, M. Hara, H. Kobayashi, K. Domen, Y. Inoue, RuO 2 -loaded β-Ge 3 N 4 as a non-oxide photocatalyst for overall water splitting, J. Am. Chem. Soc. 127 (12) (2005) 4150–4151.

[7] M.Z. Ansari, D.K. Nandi, R. Janicek, S.A. Ansari, R. Ramesh, R.T. Cheon, B. Shong, S.-H. Kim, Low-temperature atomic layer deposition of highly conformal tin nitride thin films for energy storage devices, ACS Appl. Mater. Interfaces 11 (2019) 43608–43621, https://doi.org/10.1021/acsami.9b15790.

[8] S. Dong, X. Chen, L. Gu, X. Zhou, H. Wang, Z. Liu, P. Han, J. Yao, L.i. Wang, G. Cui, L. Chen, TiN/VN composites with core/shell structure for supercapacitors, Mater. Res. Bull. 46 (6) (2011) 835–839.

[9] Q. Sun, Z.-W. Fu, Vanadium nitride as a novel thin film anode material for rechargeable lithium batteries, Electrochim. Acta 54 (2) (2008) 403–409.

[10] R. Ramesh, D.K. Nandi, T.H. Kim, T. Cheon, J. Oh, S.-H. Kim, Atomic-layer-deposited MoN x thin films on three-dimensional Ni foam as efficient catalysts for the electrochemical hydrogen evolution reaction, ACS Appl. Mater. Interfaces 11 (19) (2019) 17321–17332.

[11] D.K. Nandi, S. Sahoo, T.H. Kim, T. Cheon, S. Sinha, R. Rahul, Y. Jang, J.-S. Bae, J. Heo, J.-J. Shim, S.-H. Kim, Low temperature atomic layer deposited molybdenum nitride-Ni-foam composite: an electrode for efficient charge storage, Electrochem. Commun. 93 (2018) 114–118.

[12] F. Qu, Y. Yuan, M. Yang, Programmed synthesis of Sn 3 N 4 nanoparticles via a soft chemistry approach with urea: application for ethanol vapor sensing, Chem. Mater. 29 (3) (2017) 969–974.

[13] X. Li, A.L. Hector, J.R. Owen, S.I.U. Shah, Evaluation of nanocrystalline Sn 3 N 4 derived from ammonolysis of Sn(NEt 2) 4 as a negative electrode material for Li-ion and Na-ion batteries, J. Mater. Chem. A 4 (14) (2016) 5081–5087.

[14] D. Lützenkirchen-Hecht, R. Frahm, Structure of reactively sputter deposited tin-nitride thin films: a combined X-ray photoelectron spectroscopy, in situ X-ray reflectivity and X-ray absorption spectroscopy study, Thin Solid Films 493 (1-2) (2005) 67–76.

[15] T. Maruyama, Y. Osaki, Effect of electrochemical polarization on optical properties of sputter-prepared tin nitride in aqueous electrolyte, J. Electrochem. Soc. 143 (1) (1996) 326–329.

[16] O. Takai, A new electrochromic system using tin-nitride thin films, Proc. SID 10014 (1987) 243–246.

[17] Y. Inoue, M. Nomiya, O. Takai, Physical properties of reactive sputtered tin-nitride thin films, Vacuum 51 (4) (1998) 673–676.

[18] R.G. Gordon, D.M. Hoffman, U. Riaz, Low-temperature atmospheric pressure chemical vapor deposition of polycrystalline tin nitride thin films, Chem. Mater. 4 (1) (1992) 68–71.

[19] C.M. Caskey, J.A. Seabold, V. Stevanović, M. Ma, W.A. Smith, D.S. Ginley, N.R. Neale, R.M. Richards, S. Lany, A. Zakutayev, Semiconducting properties of spinel tin nitride and other IV 3 N 4 polymorphs, J. Mater. Chem. C 3 (6) (2015) 1389–1396.

[20] N. Takahashi, M. Takekawa, T. Takahashi, T. Nakamura, M. Yoshioka, W. Inami, Y. Kawata, Optical recording characteristics of tin nitride thin films prepared by an atmospheric pressure halide chemical vapor deposition, Solid State Sci. 5 (4) (2003) 587–589.

[21] N. Takahashi, K. Terada, T. Nakamura, Atmospheric pressure chemical vapor deposition of tin nitride thin films using a halide source, J. Mater. Sci. Lett. 20 (2001) 227-228. https://doi.org/10.1039/B005032F.

[22] D.M. Hoffman, S. Prakash Rangarajan, S.D. Athavale, D.J. Economou, J.-R. Liu, Z. Zheng, W.-K. Chu, Plasma-enhanced chemical vapor deposition of silicon, germanium, and tin nitride thin films from metalorganic precursors, J. Vacuum Sci. Technol. A: Vacuum, Surf. Films 13 (3) (1995) 820–825.

[23] R.S. Lima, P.H. Dionisio, W.H. Schreiner, C. Achete, Magnetron sputtered tin nitride, Solid State Commun. 79 (5) (1991) 395–398.

[24] T. Maruyama, T. Morishita, Tin nitride thin films prepared by radio-frequency reactive sputtering, J. Appl. Phys. 77 (12) (1995) 6641–6645.

[25] L. Baggetto, N.A.M. Verhaegh, R.A.H. Niessen, F. Roozeboom, J.-C. Jumas, P.H.L. Notten, Tin nitride thin films as negative electrode material for lithium-ion solid-state batteries, J. Electrochem. Soc. 157 (2010) A340-A347. https://doi.org/10.1149/1.3290778.

[26] T. Maruyama, T. Morishita, Copper nitride and tin nitride thin films for write-once optical recording media, Appl. Phys. Lett. 69 (7) (1996) 890–891.

[27] R. Kamei, T. Migita, T. Tanaka, K. Kawabata, Effect of d.c. bias on the deposition rate using r.f.–d.c. coupled magnetron sputtering for SnN_x thin films, Vacuum 59 (2-3) (2000) 764–770.

[28] A. Garzon-Fontecha, W. De La Cruz, M. Quevedo, Electrical, optical, and structural characterization of p-type N-doped SnO thin films prepared by thermal oxidation of sputtered SnN x thin films, Surf. Interface Anal. 49 (12) (2017) 1225–1231.

[29] M. Uekubo, T. Oku, K. Nii, M. Murakami, K. Takahiro, S. Yamaguchi, T. Nakano, T. Ohta, WN_x diffusion barriers between Si and Cu, Thin Solid Films 286 (1-2) (1996) 170–175.

[30] J.B. Kim, D.K. Nandi, T.H. Kim, Y. Jang, J.-S. Bae, T.E. Hong, S.-H. Kim, Atomic layer deposition of WN_x thin films using a F-free tungsten metal-organic precursor and NH_3 plasma as a Cu-diffusion barrier, Thin Solid Films 685 (2019) 393–401.

[31] I.M. Odeh, Optical characteristics of amorphous tin nitride thin films prepared by ion beam assisted DC magnetron reactive sputtering, Jordan J. Phys. 1 (2008) 19–29.

[32] N.K. Ponon, D.J.R. Appleby, E. Arac, P.J. King, S. Ganti, K.S.K. Kwa, A. O'Neill, Effect of deposition conditions and post deposition anneal on reactively sputtered titanium nitride thin films, Thin Solid Films 578 (2015) 31–37.

[33] P.h. Roquiny, F. Bodart, G. Terwagne, Colour control of titanium nitride coatings produced by reactive magnetron sputtering at temperature less than 100°C, Surf. Coat. Technol. 116-119 (1999) 278–283.

[34] S.M. George, Atomic layer deposition: an overview, Chem. Rev. 110 (1) (2010) 111–131.

[35] M.Z. Ansari, N. Parveen, D.K. Nandi, R. Ramesh, S.A. Ansari, T. Cheon, S.-H. Kim, Enhanced activity of highly conformal and layered tin sulfide (SnS_x) prepared by atomic layer deposition (ALD) on 3D metal scaffold towards high performance supercapacitor electrode, Sci Rep 9 (1) (2019), https://doi.org/10.1038/s41598-019-46679-7.

[36] N. Haberkorn, S. Bengio, H. Troiani, S. Suárez, P.D. Pérez, M. Sirena, J. Guimpel, Synthesis of nanocrystalline δ-MoN by thermal annealing of amorphous thin films grown on (100) Si by reactive sputtering at room temperature, Thin Solid Films 660 (2018) 242–246.

[37] K. Khojier, M. Reza, K. Mehr, H. Savaloni, Annealing temperature effect on the mechanical and tribological properties of molybdenum nitride thin films, J Nanostruct Chem 5 (2013), https://doi.org/10.1186/2193-8865-3-5.

[38] P.L. Moharana, S. Anwar, A. Islam, S. Anwar, Structural and mechanical study of thermally annealed tungsten nitride thin films, Perspect. Sci. 8 (2016) 636–638.

[39] M. Grosser, M. Münch, H. Seidel, C. Bienert, A. Roosen, U. Schmid, The impact of substrate properties and thermal annealing on tantalum nitride thin films, Appl. Surf. Sci. 258 (7) (2012) 2894–2900.

[40] Y.M. Lu, R.J. Weng, W.S. Hwang, Y.S. Yang, Study of phase transition and electrical resistivity of tantalum nitride films prepared by DC magnetron sputtering with OES detection system, Thin Solid Films 398-399 (2001) 356–360.

[41] H. Gueddaoui, G. Schmerber, Effect of annealing on the structural and optical properties of sputtered HfN_x thin films, Int. J. Nanoparticles 6 (2013), https://doi.org/10.1504/IJNP.2013.054991.

[42] J.S.C. Kearney, M. Graužinytė, D. Smith, D. Sneed, C. Childs, J. Hinton, C. Park, J.S. Smith, E. Kim, S.D.S. Fitch, A.L. Hector, C.J. Pickard, J.A. Flores-Livas, A. Salamat, Pressure-tuneable visible-range band gap in the ionic spinel tin nitride, Angew. Chem. 130 (36) (2018) 11797–11802.

[43] E. Lewin, J. Patscheider, Structure and properties of sputter-deposited Al-Sn-N thin films, J. Alloy. Compd. 682 (2016) 42–51.

[44] N. Scotti, W. Kockelmann, J. Senker, S. Trabel, H. Jacobs, Sn_3N_4, ein Zinn(IV)-nitrid - synthese underste Strukturbestimmung einer binaren Zinn-Stickstoff-Verbindung, *Z.* für Anorg. Allg. Chem. 625 (1999) 1435–1439, https://doi.org/10.1002/(SICI)1521-3749(199909)625:9<1435::AID ZAAC1435>3.0.CO;2-%23.

[45] A. Subramaniyan, J.D. Perkins, R.P. O'Hayre, D.S. Ginley, S. Lany, A. Zakutayev, Non-equilibrium synthesis, structure, and opto-electronic properties of $Cu_{2-2x}Zn_xO$ alloys, J. Mater. Sci. 50 (2015) 1350, https://doi.org/10.1007/s10853-014-8695-0.

[46] C. M. Caskey, A. Holder, S. Shulda, S. T. Christensen, D. Diercks, C. P. Schwartz, D. Biagioni, D. Nordlund, A. Kukliansky, A. Natan, D. Prendergast, B. Orvananos, W. Sun, X. Zhang, G. Ceder, D. S. Ginley, W. Tumas, J. D. Perkins, V. Stevanovic, S. Pylypenko, S. Lany, R. M. Richards, A. Zakutayev, Synthesis of a mixed-valent tin nitride and considerations of its possible crystal structures, J. Chem. Physics 144 (2016) 144201. https://doi.org/10.1063/1.4945561.

[47] L. Maya, Preparation of tin nitride via an amide-imide intermediate, Inorg. Chem. 31 (10) (1992) 1958–1960.

[48] S. Pylypenko, A. Queen, T.S. Olson, A. Dameron, K. O'Neill, K.C. Neyerlin, B. Pivovar, H.N. Dinh, D.S. Ginley, T. Gennett, R. O'Hayre, Tuning carbon-based fuel cell catalyst support structures via nitrogen functionalization. I. Investigation of structural and compositional modification of highly oriented pyrolytic graphite model catalyst supports as a function of nitrogen implantation dose, J. Phys. Chem. C 115 (28) (2011) 13667–13675.

[49] J. Torres, C.C. Perry, S.J. Bransfield, D.H. Fairbrother, Low-temperature oxidation of nitride iron surfaces, J. Phys. Chem. B 107 (2003) 5558, https://doi.org/10.1021/jp027802w.

[50] C.M. Herzinger, B. Johs, W.A. McGahan, J.A. Woollam, W. Paulson, Ellipsometric determination of optical constants for silicon and thermally grown silicon dioxide via a multi-sample, multi-wavelength, multi-angle investigation, J. Appl. Phys. 83 (6) (1998) 3323–3336.

[51] D.A.G. Bruggeman, Berechnung verschiedener physikalischer Konstanten von heterogenen substanzen, Ann. Phys. (Leipzig) 24 (1935) 636–679.

[52] G.E. Jellison, F.A. Modine, Parametrization of the optical functions of amorphous materials in the interband region, Appl. Phys. Lett. 69 (1996) 371–373, https://doi.org/10.1063/1.118155.

[53] T.E. Tiwald, D.W. Thompson, J.A. Woollam, W. Paulson, R. Hance, Application of IR variable angle spectroscopic ellipsometry to the determination of free carrier concentration depth profiles, Thin Solid Films 313-314 (1998) 661–666.

[54] W.Y. Ching, P. Rulis, Ab initio calculation of the electronic structure and spectroscopic properties of spinel γ-Sn_3N_4, Phys. Rev. B 73 (2006) 045202, https://doi.org/10.1103/PhysRevB.73.045202.

[55] E. Palik, Handbook of Optical Constants of Solids, Academic Press, 1998.

[56] S. Benramache, A. Arif, O. Belahssen, A. Guettaf, Study on the correlation between crystallite size and optical gap energy of doped ZnO thin film, J. Nanostruct. Chem. 3 (1) (2013), https://doi.org/10.1186/2193-8865-3-80.